Nature of Metal-Support Interaction Discovered by Interpretable Machine Learning

Tairan Wang[1]†, Runhai Ouyang[2]†, Jianyu Hu[3]†, Yutao Wang[1], Wu Shu[1], Xuting Chai[1], Sulei Hu[3], Wei-Xue Li[1,4]*

[1]Key Laboratory of Precision and Intelligent Chemistry, Department of Chemical Physics, School of Chemistry and Materials Science, iChem, University of Science and Technology of China; Hefei, 230026, China.

[2]Materials Genome Institute, Shanghai University; Shanghai, 200444, China.

[3]Hefei National Research Center for Physical Sciences at the Microscale, University of Science and Technology of China; Hefei, 230026, China.

[4]Hefei National Laboratory, University of Science and Technology of China; Hefei, Anhui, 230088, China.

†These authors contributed equally to this work.

*Corresponding author. Email: *wxli70@ustc.edu.cn*

Abstract: Metal catalysts supported on oxides play a paramount role in numerous industrial reactions. Modulating metal-support interaction is a key strategy to boost catalytic productivity and stability; however, the nature of metal-support interaction and quantification remain major unsolved problems. By leveraging interpretable machine learning, domain knowledge, and experimental data available, we discover a physical metal-support interaction equation applicable to metal nanoparticles and adatoms on oxides, and oxide films on metals. Though metal-oxygen interaction dominates metal-support interaction and determines the metal composition effect, metal-metal interaction delineates the support effect. This ensures a principle of strong metal-metal interaction for encapsulation of suboxide over metal nanoparticles, substantiated comprehensively by molecular dynamics simulations and previous experiments. The developed theory provides valuable insights and guidance in engineering the metal-support interface.

Introduction

Metals catalysts anchored on oxide supports form the basis of many important industrial processes, from petrochemical refining to environmental protection, driving efficiencies and sustainable solutions (*1, 2*). How metals interact with reactants in the gas phase and support underneath is vital for the catalytic activity, selectivity, and stability (*3, 4*). Metal-reactant interaction (MRI) shapes reaction steps including adsorption, diffusion, surface reaction, and desorption, and fundamental theories such as the Sabatier principle, Brønsted-Evans-Polanyi relationship, and d-band theory along with density functional theory (DFT) calculations have been developed to optimize the MRI (*5, 6*). Metal-support interaction (MSI) is decisive in stabilizing the dispersed catalysts (*7, 8*) and influencing various interface phenomena, including charge transfer, the interfacial perimeter, nanoparticle morphology, chemical composition, and encapsulation, which makes its modulation one of few tools able to enhance catalytic performance (*9, 10*). Despite extensive investigations, the nature of MSI and its structure-activity relationship remain major unsolved problems, posing a challenge for the rational design of the metal-oxide composites in heterogeneous catalysis.

To reveal the nature of MSI, various variables have been proposed, such as metal oxophilicity and activity of oxide surface oxygen (*11, 12*), metal electron density coupled with oxide's band gap (*13, 14*), metal surface energy and Van der Waals interactions (*15, 16*). However, these assessments are limited to specific metal-support archetypes and/or small datasets. Moreover, as the metal size increases from single atoms to clusters, nanoparticles (NPs) and larger structures, the types of chemical bonds involved and their competition across the interfaces change significantly (*17, 18*). The low symmetry of interfacial structures and the complexity of composition spaces further hinder the uncovering of the modulation principles of MSI (*19, 20*). Finally, quantification of MSI with predictive ability is critical for many desired catalytic consequences (*21, 22*), including sintering (*23*), but has not yet been developed. This is closely related to classic strong MSI (SMSI), an important concept proposed in 1978 (*24*) and revived recently (*25*). Rather than focusing on the term itself, "SMSI" has been used liberally to refer to the encapsulation of suboxide layers on supported metal NPs, and even all obvious interfacial phenomena, a fact that leads to wide controversies (*26*). Determining when MSI is considered strong and when encapsulation occurs is important but remains elusive.

To solve these challenges, we harnessed the power of interpretable machine learning to reveal the nature of MSI and develop a predictive theory to quantify MSI. By leveraging

symbolic regression techniques (*27*), domain knowledge, and experimental data across 25 metals and 27 oxides, an interpretable MSI equation composed of metal-oxygen interaction (MOI) and metal-metal interaction (MMI) was discovered. The nature of MSI revealed for metal NPs on oxide supports can apply to single metal adatoms on oxide supports, and oxide films on metal supports, as proved by DFT calculations. We find that MOI determines the MSI strength and metal composition effect, whereas MMI delineates the support effect. Massive molecular dynamics (MD) simulations powered by machine learning potential (*28*) reveal migration and encapsulation of suboxide layers onto metal NPs, where metal-metal bonds dominates the suboxide-metal interface, and metal-metal bonding strength determines the migration kinetics. We propose a principle that the migration is driven by, and encapsulation occurs when, the metal-metal bonding energy between the supported metal and the oxide's metal surpasses that of the oxide metals. The principle of strong MMI is substantiated by comprehensive experimental observations. Our findings offer profound insights into the MSI and constructive ways in engineering the metal-support interface for more efficient catalysts.

Discovery of Meta-Support Interaction Equation

The protocol for finding the MSI equation is schematically depicted in Fig. 1A. The adhesion energy of E_{adh} between metal particles and oxide supports is a critical variable for quantifying the MSI. We compiled E_{adh} data for 178 metal-oxide interfaces from publications, spanning 25 metals and 27 oxides, as shown in Fig. 1B and table S1. These data were consistently measured at liquid metal particles on oxides using the sessile drop method in wetting experiments. To reveal the nature of MSI, the incorporation of substantial domain knowledge is essential, and 50 relevant quantities to E_{adh} are considered (table S2). Though these parameters were proposed from different perspectives, many of them are correlated. To minimize their correlation, we performed a thorough backward elimination and cross-validation, and 14 important physical parameters with low Pearson correlations were distilled (table S3, fig. S1). Using the distilled features and prescribed operators, we employed the symbolic regression method of SISSO (*27*) to construct and explore over 30 billion mathematical expressions. Considering both parsimony and accuracy, an optimal model with two dimensions (2D) and a feature complexity of 4 was identified, exhibiting excellent accuracy across the training, validation, and test datasets, with a test root-mean-squared-error of ~14 meV/Å^2 (fig. S4, details in **Supplementary Materials (SM)**). This accuracy surpasses

that of previous descriptors (table S4) and neural network models (fig. S2), and is comparable with experimental uncertainty ranging from 6.25 to 18.75 meV/Å² (*29*).

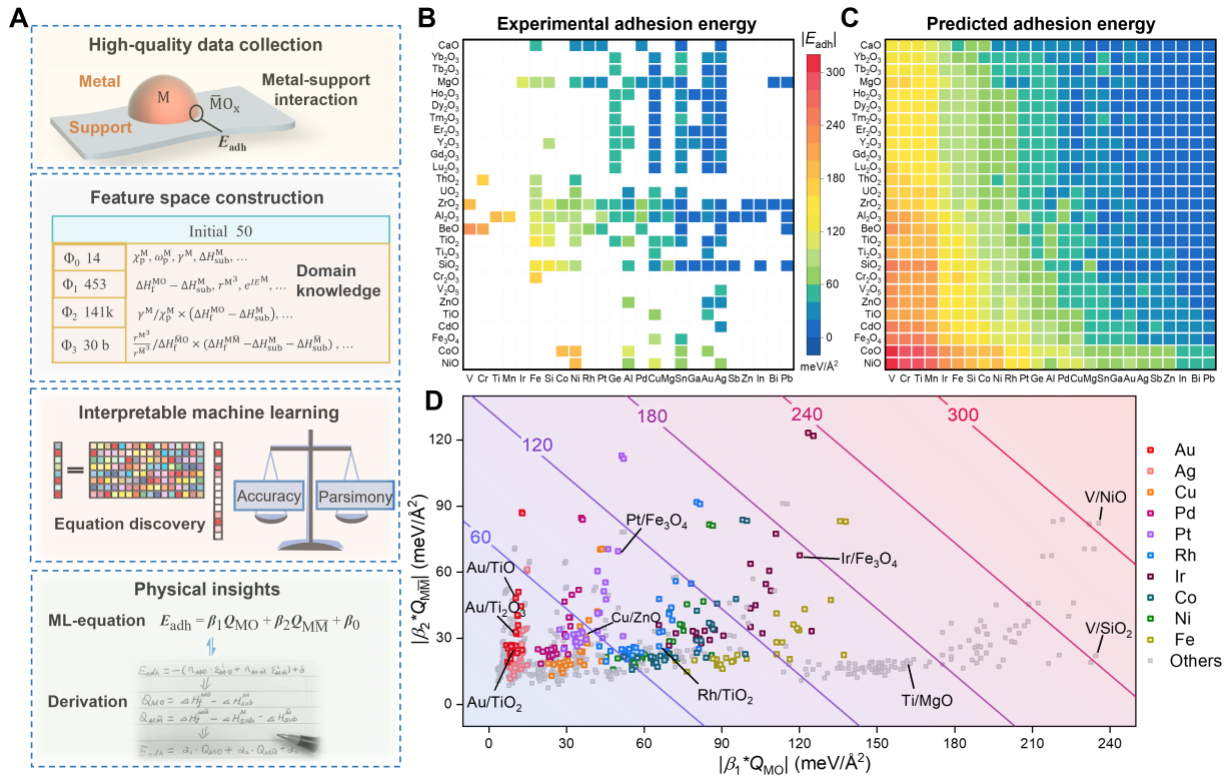

Fig. 1. Discovery of MSI equation and predictions. (A) The development of the derivable MSI equation, including data collection, feature engineering, descriptor identification, and physical derivation. (B) Collected $|E_{\mathrm{adh}}|$ of the metal-support systems (metals as x-axis and supports as y-axis) from literature. Arrangement of the metals (oxides) in the x-axis (y-axis) are done according to their $|E_{\mathrm{adh}}|$. (C) The recovered image of (B) by filling out the white spots with $|E_{\mathrm{adh}}|$ predicted by Eq. 1. (D) Distribution of the metal-oxide systems within the two-dimensional space spanned by $|\beta_2 \cdot Q_{\mathrm{M\bar{M}}}|$ and $|\beta_1 \cdot Q_{\mathrm{MO}}|$ for all the considered experimental metal-oxide systems. Contour lines denote increments of $|E_{\mathrm{adh}}|$ at 60 meV/Å². Selected catalytic systems of interest are highlighted with distinct colors and annotated.

The functional form of the optimal model is:

$$E_{\mathrm{adh}} = \beta_1 \cdot Q_{\mathrm{MO}} + \beta_2 \cdot Q_{\mathrm{M\bar{M}}} + \beta_0 \tag{1}$$

with

$$Q_{\mathrm{MO}} = \Delta H_{\mathrm{f}}^{\mathrm{MO}} - \Delta H_{\mathrm{sub}}^{\mathrm{M}},\ Q_{\mathrm{M\bar{M}}} = \Delta H_{\mathrm{f}}^{\mathrm{M\bar{M}}} - \Delta H_{\mathrm{sub}}^{\mathrm{M}} - \Delta H_{\mathrm{sub}}^{\bar{\mathrm{M}}}, \tag{2}$$

Here, superscripts M and $\bar{\mathrm{M}}$ denote the element of supported metal and the metal in oxide, respectively. ΔH_{sub} is the sublimation enthalpy, and $\Delta H_{\mathrm{f}}^{\mathrm{MO}}$ is the formation enthalpy of supported metal forming its most stable oxide. The difference, represented by Q_{MO}, is the corresponding energy gain to form the oxide with respect to gas metal atoms, manifesting the

metal's oxophilicity (*11, 12*). For the prefactor $\beta_1 = 6.09 \cdot \gamma^{\mathrm{M}} \cdot \chi_{\mathrm{p}}^{\bar{\mathrm{M}}} / \chi_{\mathrm{p}}^{\mathrm{M}}$, surface energy of γ^{M} is associated with the Van der Waals interfacial interactions, evident for weak MSI (*15*), as depicted in fig. S3. The ratio of Pauling electronegativity $\chi_{\mathrm{p}}^{\bar{\mathrm{M}}} / \chi_{\mathrm{p}}^{\mathrm{M}}$ reflects the competitive bonding of the two metal elements with oxygen, and metals with a lower χ_{p} are more prone to bond with oxygen. Similarly, $\Delta H_{\mathrm{f}}^{\mathrm{M}\bar{\mathrm{M}}}$ is the enthalpy for the mixing of $\bar{\mathrm{M}}$ in M at infinite dilution (*30*). Thus, $Q_{\mathrm{M}\bar{\mathrm{M}}}$ reflects the intrinsic bond strength between M and $\bar{\mathrm{M}}$ with respect to gas metal atoms. For the prefactor $\beta_2 = -2.85 \cdot IE^{\mathrm{M}} / \Delta H_{\mathrm{f}}^{\bar{\mathrm{M}}\mathrm{O}}$, IE^{M} is the first ionization energy of metal elements, and $\Delta H_{\mathrm{f}}^{\bar{\mathrm{M}}\mathrm{O}}$ is the formation enthalpy of the oxide support. $|\beta_2|$ is high when the metal in oxide has a weak bonding with oxygen or is in a low valent state because of low $|\Delta H_{\mathrm{f}}^{\bar{\mathrm{M}}\mathrm{O}}|$, and metal M has a weak bonding with oxygen because of high IE^{M}. β_0 is a constant of 13.33.

Employing the discovered equation allows for predictions of unknown E_{adh}. In the 2D space spanned by the oxides and metals of the considered metal-oxide composites (Fig. 1B), there were 178 known $|E_{\mathrm{adh}}|$ data and 497 unknowns. With Eq. 1, all the unknown white areas were predicted, and the "recovered image" is shown in Fig. 1C. The data is arranged in a way that the resulted $|E_{\mathrm{adh}}|$ increases from the weakest of nearly zero at the upper right to the strongest of 305 meV/Å^2 at the lower left. Systems with small $|E_{\mathrm{adh}}|$ are mainly less reactive coinage metals and p-block metals supported on irreducible oxides, such as lanthanide oxides or alkaline-earth-metal oxides. Conversely, interfaces exhibiting large $|E_{\mathrm{adh}}|$ generally feature early transition metals (TMs) supported on TM oxides. For the catalytically important group VIII metals, corresponding $|E_{\mathrm{adh}}|$ depends sensitively on the supports, varying from a weak adhesion of 20 meV/Å^2 to a strong adhesion of 240 meV/Å^2, underscoring the significant role of support effects in catalysis. With predicted E_adh, the chemical potential of metal NPs that is important for the particle reactivity is calculated for 675 metal NPs on oxides (SM).

Nature of Metal-Support Interaction

The decoupling of MSI into MOI and M$\bar{\mathrm{M}}$I provide insights that short-range chemical bonding is the main contribution to MSI. In fact, this model can be derived by assuming that MSI is shaped by the nearest-neighbor chemical bonding at the interface (**SM)**. It is written as $E_{\mathrm{adh}} = \alpha_1 \cdot Q_{\mathrm{MO}} + \alpha_2 \cdot Q_{\mathrm{M}\bar{\mathrm{M}}} + \alpha_0$, where α_1 and α_2 represent the number of interfacial M-O and M-$\bar{\mathrm{M}}$ bonds per unit area, respectively. This equation has the same functional form as that of the data-driven Eq. 1. and justifies the revealed physics: MSI is primarily determined by the MOI

and MM̄I, as described by $\beta_1 \cdot Q_{\mathrm{MO}}$ and $\beta_2 \cdot Q_{\mathrm{M\bar{M}}}$. The difference lies in the scale factors α_{i} and β_{i} and the non-chemical bonding contributions in the intercept term α_0, whereas they permeate each of the β_{i}, such as γ^{M}.

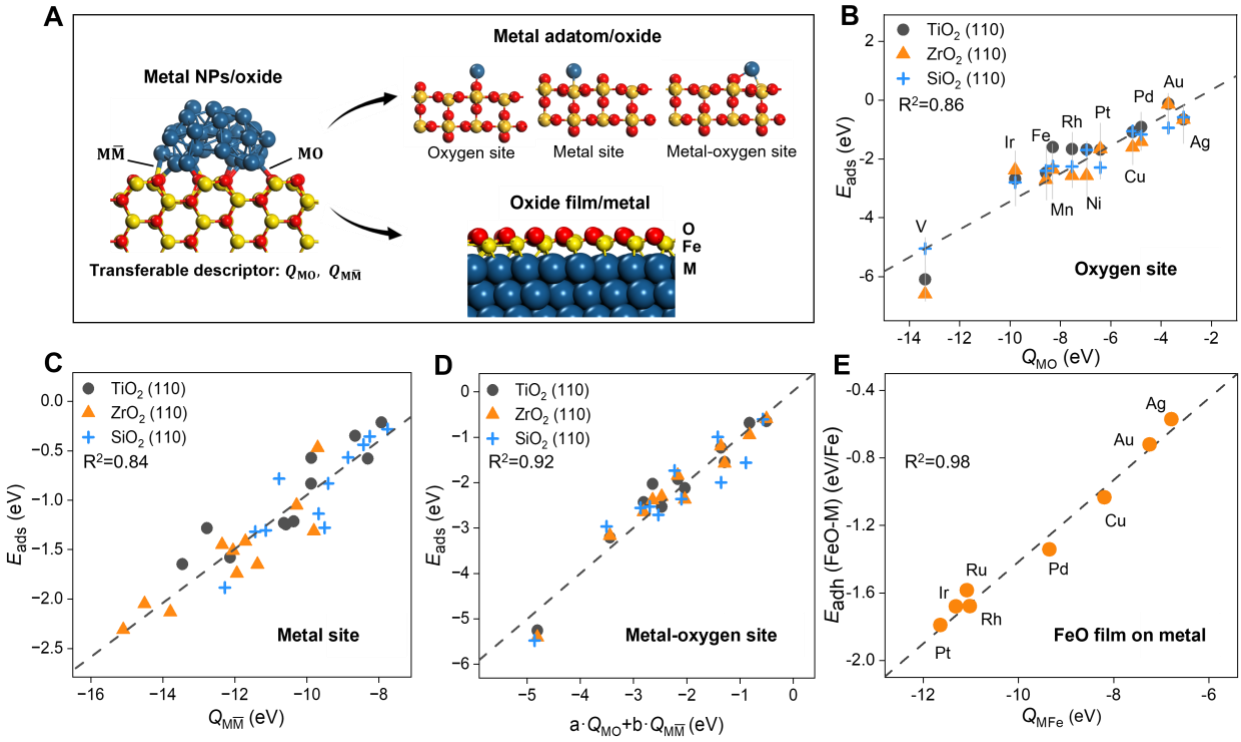

Fig. 2. Applications of data-driven insights in diverse catalytic systems. (A) Transferability of the MSI equation for metal NPs to metal adatom on oxide and oxide film on metal. The schematical structures are presented, including metal NPs on oxide, three adsorption sites of metal atom on oxide, polar interface of FeO film on metal. (B) Correlation between E_{ads} of metal adatoms on oxygen sites of TiO_2(110), ZrO_2(110) and SiO_2(110) surfaces, with the term Q_{MO}. (C) E_{ads} of metal adatom bonds only to metal atoms of oxide surfaces against $Q_{\mathrm{M\bar{M}}}$. (D) E_{ads} of metal adatom bonds with both metal and oxygen atoms on oxide surfaces against Q_{MO} and $Q_{\mathrm{M\bar{M}}}$, where a and b are fitting coefficients. (E) Calculated E_{adh}(FeO-M) (eV/Fe) against Q_{MFe} for the FeO(111)/M systems.

To single out which contributes most to MSI, we examine a 1D model with the same feature complexity of 4: $E_{\mathrm{adh}} = \sigma_1 \cdot Q_{\mathrm{MO}} + \sigma_0$, where $\sigma_1 = 3.00 \cdot \gamma^{\mathrm{M}} \cdot \chi_{\mathrm{p}}^{\bar{\mathrm{M}}} \cdot r^{\mathrm{M}}$, and $\sigma_0 = -1.62$ (see **SM**). This 1D model, aligning with previous works (*11*, *22*), emphasizes the dominant role of the Q_{MO} term. Further, projecting E_{adh} onto a 2D space spanned by $|\beta_1 \cdot Q_{\mathrm{MO}}|$ and $|\beta_2 \cdot Q_{\mathrm{M\bar{M}}}|$ in Fig. 1D reveals that the former varies up to ~240 meV/Å^2, about double that of the latter, substantiating that MOI predominates the adhesion strength. Notably, the supported Au and Ag are in the far-left domain with small $|\beta_1 \cdot Q_{\mathrm{MO}}|$, where MOI and MM̄I terms are comparable. As $|\beta_1 \cdot Q_{\mathrm{MO}}|$ increases from left to right, Cu, Pd and Pt appear, followed by Rh, Co, Ni, Ir and Fe, with V in the far-right domain where the MOI term is

overwhelmingly larger. Thus, the MOI term represents the composition effect differentiating one M from another.

Notwithstanding the predominant role of MOI, the M$\bar{\text{M}}$I term, encompassing $Q_{\text{M}\bar{\text{M}}}$ and β_2, discerns the MSI of one supported metal across various supports, namely, the support effect. To show this, we considered Au particles supported on different oxides, with the small and roughly same $|\beta_1 \cdot Q_{\text{MO}}|$ values (~10 meV/Å^2), and $|E_{\text{adh}}|$ ranges from 16 to 87 meV/Å^2 by varying $|\beta_2 \cdot Q_{\text{M}\bar{\text{M}}}|$. Particularly, for titanium oxides TiO_2, Ti_2O_3, and TiO, with the reduction in Ti valence states and $|\Delta H_{\text{f}}^{\bar{\text{M}}\text{O}}|$, $|\beta_2|$ increases from 0.94 to 1.17 and then to 1.71, and $|Q_{\text{M}\bar{\text{M}}}|$ (Au-Ti) remains constant at 9.88 eV. Consequently, $|E_{\text{adh}}|$ increases from 24 to 30 and then to 45 meV/Å^2, indicating that the higher the metallics on the oxide surface, the stronger MSI toward the Au NPs. Indeed, for coinage catalysts with relatively weak MOI, enhancing M$\bar{\text{M}}$I by exposing metal-rich surfaces, and introducing more oxygen vacancies in supports are effective strategies to strengthen the overall MSI (*31*, *32*). For Pt on various oxides, although $|\beta_1 \cdot Q_{\text{MO}}|$ increases and varies from 27 to 52 meV/Å^2, the increase of $|\beta_2 \cdot Q_{\text{M}\bar{\text{M}}}|$ is more considerable, varying from 25 to 113 meV/Å^2. This again highlights the importance of M$\bar{\text{M}}$I to the support effect for late TMs.

The physics underlined in Eq. 1 ensures the transferability of the data-driven descriptors to different interfacial systems (Fig. 2A), for instance, the adsorption of metal adatoms on oxides, whose energetics are important in single atom catalysis (*33*) and Ostwald ripening (*23*). Unlike particle adhesion, which necessitates additional features such as those in β_{i} to capture complex interactions, adsorptions of single atoms with well-defined configurations could be characterized straightforwardly by Q_{MO} and $Q_{\text{M}\bar{\text{M}}}$. To illustrate this, we performed DFT calculations for adsorption energies E_{ads} of TM adatoms on TiO_2(110), ZrO_2(110), and SiO_2(110) (**SM**). When M atoms are adsorbed at oxygen-oxygen bridge sites, bonding exclusively with surface O, E_{ads} is linearly correlated with Q_{MO} in Fig. 2B. Similarly, for M atoms located at metal-metal bridge sites, where only metal-metal interaction exists, E_{ads} correlates linearly with $Q_{\text{M}\bar{\text{M}}}$ (Fig. 2C). When M atoms are at metal-oxygen bridge sites, involving both M-O and M-$\bar{\text{M}}$ bonding, E_{ads} can be a linear combination of Q_{MO} and $Q_{\text{M}\bar{\text{M}}}$ (Fig. 2D).

The robustness of the identified descriptors extends to inverse oxide/metal catalysts, which often act as model systems for studying "SMSI" and encapsulation (*34*). Here, we study the well-documented FeO(111) bilayer film on close-packed late TM surfaces (*35*, *36*), and

corresponding E_{adh} between FeO and TM were calculated (**SM**). The optimized structures based on realistic Moiré superstructures (fig. S9) show that the FeO bilayer directly bonds with the underlying TMs, while an oxygen layer caps the Fe layer. This configuration suggests that interfacial adhesion is governed by the M-Fe interaction, namely, $Q_{M\bar{M}}$. Therefore, the calculated E_{adh} should be linearly dependent on $Q_{M\bar{M}}$, as confirmed in Fig. 2E. Among others, FeO(111) films exhibit strong adhesion to Pt, Rh, Ir, Ru, and Pd exceeding 1.34 eV per Fe atom (175 meV/Å^2), while demonstrating much weaker adhesion to Ag and Au, with a maximum of 0.72 eV per Fe atom (77 meV/Å^2). Note that encapsulation was found for Pt and Pd NPs on Fe_3O_4 when reduced in H_2 at high temperature, but not for Cu, Ag and Au (*37*, *38*). This indicates that $Q_{M\bar{M}}$ might be crucial for the encapsulation phenomenon, as discussed below.

Principle of Strong Metal-Metal Interaction

According to the Young–Dupré equation, $|E_{adh}| = \gamma^M(1 + \cos\alpha)$, adhesion strength can be strong for metals with higher γ^M, though their interfacial interaction remains weak with an obtuse contact angle α. For a given metal, strong MSI along with acute α tends to initiate Ostwald ripening, whereas weak MSI with obtuse α tends to trigger the particle migration and coalescences (*23*). When MSI is neither too strong nor too weak, with an optimum α of ~90°, thermal resistance to sintering is maximized. Based on the Young–Dupré equation, we calculated α for 675 metal-oxide interfaces (Fig. 3A), increasing from near 0° at the lower left to ~ 150° at the upper right. The most used TM catalysts predominantly occupy the right plane with obtuse angles. Specifically, for group VIII precious metals, α mainly ranges from 80° to 120°, which is fortunately close to the optimal α of ~90°. By contrast, Cu, Ag, and Au are more likely to exhibit weaker MSI with most α exceeding 120° and prone to sintering, which could be mitigated by enhancing the MSI (*39*, *40*).

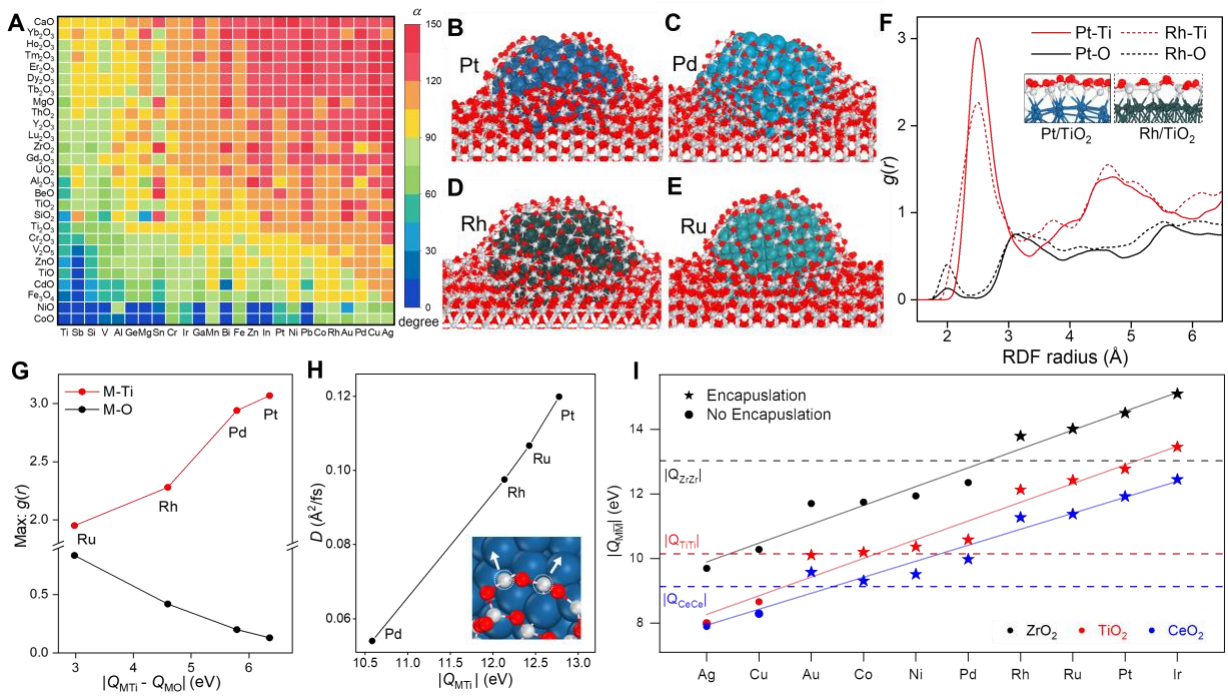

Fig. 3. Contact angles, strong metal-metal interaction, and encapsulation states. (A) Predicted contact angles α of all the 675 metal-oxide interfaces. The metals (oxides) in the x-axis (y-axis) are arranged by averaged α. (B-E) The MD-simulated SMSI states of the 305-atom Pt, Pd, Rh, and Ru NPs supported on TiO_2(110) with 12.5% oxygen vacancies at 0.8 ns of annealing at 1500 K. Red: O atoms; gray: Ti atoms. (F) Radial distribution function (RDF) of the annealed Pt/TiO_2 and Rh/TiO_2; the inset zooms are the overlayer structures. (G) Intensity of the first peaks of M-Ti and M-O bonds in RDF against $|Q_{\mathrm{MTi}} - Q_{\mathrm{MO}}|$. (H) Diffusion coefficients of Ti atoms for the migration forming the encapsulation films against $|Q_{\mathrm{MTi}}|$; the inset shows a snap of the migration. (I) The $|Q_{\mathrm{M\bar{M}}}|$ of different metals on ZrO_2, TiO_2, and CeO_2; horizon dashed lines for corresponding $|Q_{\bar{\mathrm{M}}\bar{\mathrm{M}}}|$ of three oxide supports; solid lines for guiding eyes; stars for systems reported to observe the encapsulation phenomenon, and circles for the systems without encapsulation evidence yet.

For classic "SMSI" and encapsulation phenomena, we investigated the structural evolution of Pt, Rh, Pd, Ru, Cu and Ag NPs (~3 nm in diameter) on pristine rutile TiO_2(110) using MLPMD. Calculated α are obtuse angles from 106° to 132°, indicating weak MSIs. To model reduction conditions without including reductants explicitly, as an approximation, 12.5% oxygen vacancies on TiO_2(110) were introduced before annealing. For Pt, Rh, Pd and Ru NPs, with significant $|Q_{\mathrm{MTi}}|$ (10.59 eV at least), migration of Ti and O atoms onto the NP surfaces was found during the 0.8 ns simulations, eventually forming an encapsulating suboxide thin overlayer (Fig. 3B-E). Experimentally, encapsulation was indeed found in these systems (*34*, *41-43*). In contrast, for Cu and Ag NPs, with relatively weak $|Q_{\mathrm{MTi}}|$ (8.66 eV in maximum), such migration was not evident within the simulation timeframe (fig. S16), and no

encapsulation evidence was reported either. This trend highlights the importance of the strong M$\bar{M}$I in forming encapsulation layers.

For Pt and Pd on TiO_2(110), MLMD simulations show that the encapsulation layer is a single TiO_{2-x} overlayer. Corresponding Ti:O ratios vary from 1:1 to 2:3, indicating thepresence of reduced Ti^{n+} species with $1 \leq n \leq 3$ (Fig. 3B and 3C), consistent with experiments (*43-45*). The calculated radial distribution function (RDF) in Fig. 3F shows that the interface between the TiO_{2-x} overlayer and Pt NPs is primarily composed of Pt-Ti bonds. In Fig. 3B, there are Ti atoms permeating into the Pt NP, indicating the formation of Pt-Ti alloys. Indeed, significant Pt-Ti metal signals at the interface between the overlayer and metal NP have been observed, and the migration of TiO_{2-x} with limited thickness and alloy formation are competitive processes (*43*). For Rh NPs, the primary bond between the TiO_{2-x} overlayer and Rh NPs remains Rh-Ti bonds, though no Ti atoms permeating in Rh NPs was observed (Fig. 3D). The corresponding bond length averages 2.54 Å (Fig. 3F), in excellent agreement with the measured 2.53 Å (*46*). This bond length, much shorter than the 2.68 Å observed in Rh-Ti intermetallic compounds (*47*), reflects the cationic nature of Ti involved. The calculated average coordination number for Rh-Ti bonds at the interface is 1.98, aligning well with the experimental value of 1.9 (*46*).

As indicated in Fig. 3F, the first peak of the M-O bond in RDF is situated in the M-Ti shell. These M-O and M-Ti bonds constitute the interface, and their populations are decided by the difference between M$\bar{M}$I and MOI bonding, $|Q_{\mathrm{MTi}} - Q_{\mathrm{MO}}|$. Ru/$TiO_2$, with the smallest $|Q_{\mathrm{MTi}} - Q_{\mathrm{MO}}|$, displays a considerable number of M-O bonds at the interface, though fewer than the Ru-Ti bonds. Conversely, Pt/TiO_2, with the largest $|Q_{\mathrm{MTi}} - Q_{\mathrm{MO}}|$, exhibits dominant M-Ti bonds with negligible M-O bonds. Indeed, as plotted in Fig. 3G, with an increase of $|Q_{\mathrm{MTi}} - Q_{\mathrm{MO}}|$, the intensity of the M-Ti bonds increases at the expense of the M-O bonds. Notably, the migration of the TiO_{2-x} overlayer on NP surfaces is led by Ti atoms, and corresponding diffusion coefficients D_e were calculated to represent the encapsulation kinetics, which depends linearly on $|Q_{\mathrm{MTi}}|$ (Fig. 3H). Specifically, compared to Pd ($|Q_{\mathrm{MTi}}|$=10.58 eV), the calculated D_e for Pt ($|Q_{\mathrm{MTi}}|$=12.78 eV) is two times higher. Namely, the stronger the M-Ti bonds, the faster the TiO_{2-x} film migrates over NPs, since strong M$\bar{M}$I facilitates the migration of $\bar{M}$ atoms on M surfaces.

Strong M$\bar{M}$I alone does not necessarily trigger migration and encapsulation. For Pd and Ni on TiO_2, corresponding $|Q_{M\bar{M}}|$ are strong (10.37 and 10.58 eV, respectively), and

encapsulation was observed (*48-50*). However, for ZrO_2, despite enhanced $|Q_{M\bar{M}}|$ (~2 eV higher, table S7), encapsulation has not yet been reported. This enhancement in $|Q_{M\bar{M}}|$ is attributed to the more active nature of Zr metal compared to Ti, as evidenced by its large $|Q_{\bar{M}\bar{M}}|$ (13.03 eV versus 10.20 eV). In other words, too strong $|Q_{\bar{M}\bar{M}}|$ would prevent encapsulation. To overcome the limitation, stronger $M\bar{M}I$, for instance, than $\bar{M}\bar{M}I$ might be required. To explore this, Fig. 3I plots $|Q_{M\bar{M}}|$ against late TMs on ZrO_2, TiO_2, and CeO_2, alongside experimental results. Significantly, encapsulation occurs only when

$$|Q_{M\bar{M}}| > |Q_{\bar{M}\bar{M}}| \quad (3)$$

On ZrO_2, TiO_2, and CeO_2 supports, Ir, Pt, Ru and Rh exhibit overwhelmingly strong $|Q_{M\bar{M}}|$ and stronger than $|Q_{\bar{M}\bar{M}}|$, resulting in encapsulation. In contrast, Ag and Cu have weak $|Q_{M\bar{M}}|$ consistently lower than $|Q_{\bar{M}\bar{M}}|$, preventing encapsulation. For Pd, Ni, Co, and Au, with intermediate $|Q_{M\bar{M}}|$, their relative strengths versus $|Q_{\bar{M}\bar{M}}|$ become sensitive to the oxides. As shown in Fig. 3I, from CeO_2 to TiO_2 and then to ZrO_2, the corresponding $|Q_{\bar{M}\bar{M}}|$ increases from 9.04 to 13.03 eV, thereby enlarging the window for $|Q_{M\bar{M}}| > |Q_{\bar{M}\bar{M}}|$. This happens for Pd and Ni on ZrO_2 and becomes susceptible for Co and Au on TiO_2 and CeO_2. We therefore put forth a principle that when the metal-metal bonding energy between the supported metal and the oxide's metal surpasses that of the oxide metals, migration of suboxide overlayers on supported metal NPs is driven, and encapsulation phenomenon occurs. This process, driven by MMI, a component of MSI, is neither the strong MSI itself nor its direct consequence.

Acknowledgments: We thank C. T. Campbell for comments.

Funding:

Natural Science Foundation of China (22221003, 22173058, 2237020074)

Strategic Priority Research Program of the Chinese Academy of Sciences (XDB0450102)

National Key R&D Program of China (2021YFB3502000)

National Program for Support of Top-notch Young Professional

Innovation Program for Quantum Science and Technology (2021ZD0303302)

Fundamental Research Funds for the Central Universities (20720220009)

Supercomputer Center of University of Science and Technology of China and Hefei advanced computing center

Competing interests: Authors declare that they have no competing interests.

Data and materials availability: All data needed to evaluate the conclusions are present in the paper and the supplementary materials.

Supplementary Materials

Materials and Methods

Supplementary Text

Figs. S1 to S22

Tables S1 to S7

References (51-131)

References and Notes

1. L. Liu, A. Corma, Metal catalysts for heterogeneous catalysis: from single atoms to nanoclusters and nanoparticles. *Chem. Rev.* **118**, 4981-5079 (2018).
2. L. Zhang, M. Zhou, A. Wang, T. Zhang, Selective Hydrogenation over Supported Metal Catalysts: From Nanoparticles to Single Atoms. *Chem. Rev.* **120**, 683-733 (2020).
3. B. Roldan Cuenya, Metal nanoparticle catalysts beginning to shape-up. *Acc. Chem. Res.* **46**, 1682-1691 (2013).
4. C. Vogt, B. M. Weckhuysen, The concept of active site in heterogeneous catalysis. *Nat. Rev. Chem.* **6**, 89-111 (2022).
5. A. J. Medford, A. Vojvodic, J. S. Hummelshøj, J. Voss, F. Abild-Pedersen, F. Studt, T. Bligaard, A. Nilsson, J. K. Nørskov, From the Sabatier principle to a predictive theory of transition-metal heterogeneous catalysis. *J. Catal.* **328**, 36-42 (2015).
6. F. Calle-Vallejo, J. Tymoczko, V. Colic, Q. H. Vu, M. D. Pohl, K. Morgenstern, D. Loffreda, P. Sautet, W. Schuhmann, A. S. Bandarenka, Finding optimal surface sites on heterogeneous catalysts by counting nearest neighbors. *Science* **350**, 185-189 (2015).
7. Y. Dai, P. Lu, Z. Cao, C. T. Campbell, Y. Xia, The physical chemistry and materials science behind sinter-resistant catalysts. *Chem. Soc. Rev.* **47**, 4314-4331 (2018).
8. T. W. Hansen, A. T. DeLaRiva, S. R. Challa, A. K. Datye, Sintering of Catalytic Nanoparticles: Particle Migration or Ostwald Ripening? *Acc. Chem. Res.* **46**, 1720-1730 (2013).
9. T. W. van Deelen, C. Hernández Mejía, K. P. de Jong, Control of metal-support interactions in heterogeneous catalysts to enhance activity and selectivity. *Nat. Catal.* **2**, 955-970 (2019).
10. M. Monai, K. Jenkinson, A. E. M. Melcherts, J. N. Louwen, E. A. Irmak, S. Van Aert, T. Altantzis, C. Vogt, W. van der Stam, T. Duchoň, B. Šmíd, E. Groeneveld, P. Berben, S. Bals, B. M. Weckhuysen, Restructuring of titanium oxide overlayers over nickel nanoparticles during catalysis. *Science* **380**, 644-651 (2023).
11. S. L. Hemmingson, C. T. Campbell, Trends in adhesion energies of metal nanoparticles on oxide surfaces: understanding support effects in catalysis and nanotechnology. *ACS Nano.* **11**, 1196-1203 (2017).
12. N. J. O'Connor, A. Jonayat, M. J. Janik, T. P. Senftle, Interaction trends between single metal atoms and oxide supports identified with density functional theory and statistical learning. *Nat. Catal.* **1**, 531-539 (2018).
13. J. Li, Role of electron density of liquid metals and bandgap energy of solid ceramics on the work of adhesion and wettability of metal-ceramic systems. *J. Mater. Sci. Lett.* **11**, 903-905 (1992).
14. K. Tan, M. Dixit, J. Dean, G. Mpourmpakis, Predicting Metal–Support Interactions in Oxide-Supported Single-Atom Catalysts. *Ind. Eng. Chem. Res.* **58**, 20236-20246 (2019).
15. F. Didier, J. Jupille, The van der Waals contribution to the adhesion energy at metal-oxide interfaces. *Surf. Sci.* **314**, 378-384 (1994).
16. C. J. Bartel, S. L. Millican, A. M. Deml, J. R. Rumptz, W. Tumas, A. W. Weimer, S. Lany, V. Stevanović, C. B. Musgrave, A. M. Holder, Physical descriptor for the Gibbs energy of inorganic crystalline solids and temperature-dependent materials chemistry. *Nat. Commun.* **9**, 4168 (2018).
17. C. T. Campbell, S. C. Parker, D. E. Starr, The effect of size-dependent nanoparticle energetics on catalyst sintering. *Science* **298**, 811-814 (2002).
18. B. Qiao, A. Wang, X. Yang, L. F. Allard, Z. Jiang, Y. Cui, J. Liu, J. Li, T. Zhang, Single-atom catalysis of CO oxidation using Pt1/FeOx. *Nat. Chem.* **3**, 634-641 (2011).
19. H. Frey, A. Beck, X. Huang, J. A. v. Bokhoven, M. G. Willinger, Dynamic interplay

between metal nanoparticles and oxide support under redox conditions. *Science* **376**, 982-987 (2022).
20. V. Muravev, A. Parastaev, Y. van den Bosch, B. Ligt, N. Claes, S. Bals, N. Kosinov, E. J. M. Hensen, Size of cerium dioxide support nanocrystals dictates reactivity of highly dispersed palladium catalysts. *Science* **380**, 1174-1179 (2023).
21. Y. Suchorski, S. M. Kozlov, I. Bespalov, M. Datler, D. Vogel, Z. Budinska, K. M. Neyman, G. Rupprechter, The role of metal/oxide interfaces for long-range metal particle activation during CO oxidation. *Nat. Mater.* **17**, 519-522 (2018).
22. C. T. Campbell, Z. Mao, Chemical potential of metal atoms in supported nanoparticles: dependence upon particle size and support. *ACS Catal.* **7**, 8460-8466 (2017).
23. S. Hu, W.-X. Li, Sabatier principle of metal-support interaction for design of ultrastable metal nanocatalysts. *Science* **374**, 1360-1365 (2021).
24. S. Tauster, S. Fung, R. L. Garten, Strong metal-support interactions. Group 8 noble metals supported on titanium dioxide. *J. Am. Chem. Soc.* **100**, 170-175 (1978).
25. M. Xu, M. Peng, H. Tang, W. Zhou, B. Qiao, D. Ma, Renaissance of Strong Metal–Support Interactions. *J. Am. Chem. Soc.* **146**, 2290-2307 (2024).
26. T. Pu, W. Zhang, M. Zhu, Engineering heterogeneous catalysis with strong metal–support interactions: Characterization, theory and manipulation. *Angew. Chem. Int. Ed. Engl.* **62**, e202212278 (2023).
27. R. Ouyang, S. Curtarolo, E. Ahmetcik, M. Scheffler, L. M. Ghiringhelli, SISSO: A compressed-sensing method for identifying the best low-dimensional descriptor in an immensity of offered candidates. *Phys. Rev. Mater.* **2**, 083802 (2018).
28. S. D. Huang, C. Shang, P. L. Kang, X. J. Zhang, Z. P. Liu, LASP: Fast global potential energy surface exploration. *Wiley Interdiscip. Rev. Comput. Mol. Sci.* **9**, e1415 (2019).
29. C. T. Campbell, J. R. Sellers, Anchored metal nanoparticles: Effects of support and size on their energy, sintering resistance and reactivity. *Faraday Discuss.* **162**, 9-30 (2013).
30. N. Eustathopoulos, B. Drevet, Determination of the nature of metal–oxide interfacial interactions from sessile drop data. *Mater. Sci. Eng. A* **249**, 176-183 (1998).
31. Y. Wang, D. Widmann, M. Heenemann, T. Diemant, J. Biskupek, R. Schlögl, R. J. Behm, The role of electronic metal-support interactions and its temperature dependence: CO adsorption and CO oxidation on Au/TiO2 catalysts in the presence of TiO2 bulk defects. *J. Catal.* **354**, 46-60 (2017).
32. A. Ruiz Puigdollers, P. Schlexer, S. Tosoni, G. Pacchioni, Increasing Oxide Reducibility: The Role of Metal/Oxide Interfaces in the Formation of Oxygen Vacancies. *ACS Catal.* **7**, 6493-6513 (2017).
33. A. Wang, J. Li, T. Zhang, Heterogeneous single-atom catalysis. *Nat. Rev. Chem.* **2**, 65-81 (2018).
34. X. Wang, A. Beck, J. A. van Bokhoven, D. Palagin, Thermodynamic insights into strong metal–support interaction of transition metal nanoparticles on titania: simple descriptors for complex chemistry. *J. Mater. Chem. A* **9**, 4044-4054 (2021).
35. M. Shipilin, E. Lundgren, J. Gustafson, C. Zhang, F. Bertram, C. Nicklin, C. J. Heard, H. Grönbeck, F. Zhang, J. Choi, Fe Oxides on Ag Surfaces: Structure and Reactivity. *Top. Catal.* **60**, 492-502 (2017).
36. Q. Fu, W. X. Li, Y. Yao, H. Liu, H. Y. Su, D. Ma, X. K. Gu, L. Chen, Z. Wang, H. Zhang, B. Wang, X. Bao, Interface-confined ferrous centers for catalytic oxidation. *Science* **328**, 1141-1144 (2010).
37. P. Wu, S. Tan, J. Moon, Z. Yan, V. Fung, N. Li, S.-Z. Yang, Y. Cheng, C. W. Abney, Z. Wu, Harnessing strong metal–support interactions via a reverse route. *Nat. Commun.* **11**, 3042 (2020).
38. S. Kaiser, J. Plansky, M. Krinninger, A. Shavorskiy, S. Zhu, U. Heiz, F. Esch, B. A.

Lechner, Does Cluster Encapsulation Inhibit Sintering? Stabilization of Size-Selected Pt Clusters on Fe3O4 (001) by SMSI. *ACS Catal.* **13**, 6203-6213 (2023).
39. J. Zhang, J. Ma, T. S. Choksi, D. Zhou, S. Han, Y.-F. Liao, H. B. Yang, D. Liu, Z. Zeng, W. Liu, Strong metal–support interaction boosts activity, selectivity, and stability in electrosynthesis of H2O2. *J. Am. Chem. Soc.* **144**, 2255-2263 (2022).
40. W. Cai, X. Sun, Y. Bao, J. Guo, A. Liu, K. Hu, L. Feng, Distinct morphology-dependent behaviors for Au/γ-Al 2 O 3 catalysts: enhanced thermal stabilization in CO oxidation reaction. *RSC Adv.* **13**, 9010-9019 (2023).
41. S. C. Fung, XPS studies of strong metal-support interactions (SMSI)—PtTiO2. *J. Catal.* **76**, 225-230 (1982).
42. J. A. Horsley, A molecular orbital study of strong metal-support interaction between platinum and titanium dioxide. *J. Am. Chem. Soc.* **101**, 2870-2874 (1979).
43. A. Beck, X. Huang, L. Artiglia, M. Zabilskiy, X. Wang, P. Rzepka, D. Palagin, M.-G. Willinger, J. A. van Bokhoven, The dynamics of overlayer formation on catalyst nanoparticles and strong metal-support interaction. *Nat. Commun.* **11**, 3220 (2020).
44. F. Pesty, H.-P. Steinrück, T. E. Madey, Thermal stability of Pt films on TiO2(110): evidence for encapsulation. *Surf. Sci.* **339**, 83-95 (1995).
45. S. Zhang, P. N. Plessow, J. J. Willis, S. Dai, M. Xu, G. W. Graham, M. Cargnello, F. Abild-Pedersen, X. Pan, Dynamical Observation and Detailed Description of Catalysts under Strong Metal-Support Interaction. *Nano. Lett.* **16**, 4528-4534 (2016).
46. S. Sakellson, M. McMillan, G. L. Haller, EXAFS evidence for direct metal-metal bonding in reduced rhodium/titania catalysts. *J. Phys. Chem.* **90**, 1733-1736 (1986).
47. D. Koningsberger, J. Martens, R. Prins, D. Short, D. Sayers, The structure of a rhodium/titania catalyst in the strong metal-support interaction state as determined by EXAFS. *J. Phys. Chem.* **90**, 3047-3050 (1986).
48. J. Sá, J. Bernardi, J. A. Anderson, Imaging of low temperature induced SMSI on Pd/TiO 2 catalysts. *Catal. Lett.* **114**, 91-95 (2007).
49. M. Monai, K. Jenkinson, A. E. Melcherts, J. N. Louwen, E. A. Irmak, S. Van Aert, T. Altantzis, C. Vogt, W. van der Stam, T. Duchoň, Restructuring of titanium oxide overlayers over nickel nanoparticles during catalysis. *Science* **380**, 644-651 (2023).
50. X. Du et al., Size-dependent strong metal-support interaction in TiO2 supported Au nanocatalysts. *Nat. Commun*. **11**, 5811 (2020).